Full-scale collapse testing of a steel stiffened plate structure under axial-compressive loading at a temperature of -80ºC

Jeom Kee Paik[a,b,c], Dong Hun Lee[c], Dae Kyeom Park[b] and Jonas W. Ringsberg[d]

[a] Department of Mechanical Engineering, University College London, London, UK; [b] The Korea Ship and Offshore Research Institute (The International Centre for Advanced Safety Studies, The Lloyd′s Register Foundation Research Centre of Excellence), Pusan National University, Busan, South Korea; [c] Department of Naval Architecture and Ocean Engineering, Pusan National University, Busan, South Korea; [d] Department of Mechanics and Maritime Sciences, Chalmers University of Technology, Göteborg, Sweden

[*] Corresponding author. J.K. Paik, Email: j.paik@ucl.ac.uk

Abstract

The aim of the paper was to develop a test database of the ultimate strength characteristics of full-scale steel stiffened plate structures under axial compressive loading at a temperature of -80ºC. This paper is a sequel to the authors' articles (Paik et al. 2020a, https://doi.org/10.1016/j.istruc.2020.05.026 and Paik et al. 2020b, https://doi.org/10.1080/17445302.2020.1787930). In contrast to the earlier articles associated with room temperature or cryogenic condition, this paper investigated the effect of a low temperature at -80ºC which is within the boundary rage of temperature of the ductile-to-brittle fracture transition for carbon steels. A material model representing the test conditions was also proposed to capture the characteristics of carbon steels at low temperatures both in tension and in compression, and it was used in finite element method simulations of the full-scale experiment. A comparison between numerical analyses and experiments showed that the proposed model could successfully predict the failure modes and ultimate strength characteristics at low temperatures for stiffened plate structures under axial compressive loading conditions.

Keywords: Ductile-to-brittle fracture transition temperature, full-scale collapse testing, low temperature, cryogenic condition, steel stiffened plate structures, ultimate compressive strength.

1. Introduction

Steel stiffened panels are used in naval, offshore, mechanical and civil engineering structures as primary strength members of ships, offshore structures and bridges. They are rarely exposed to low temperatures or cryogenic condition due to unwanted release of liquefied gas such as liquefied natural gas (LNG) or liquefied hydrogen (Paik 2019, Paik et al. 2020b). Ultimate strength is dealt with as a primary criterion of structural design (Hughes and Paik 2013, Paik 2018), and thus it is important to

characterize the effect of low temperatures on the ultimate strength of steel stiffened panels, among other parameters.

The environmental conditions of engineering structures in the range of -40°C to -80°C are associated with the Arctic region where the average ambient temperature is -40°C in winter season, and the lowest temperature is reported to be -68°C, or exposure to low temperatures sometimes after liquefied gases are released and evaporated. Experimental studies of structural strength at low temperature conditions are found in the literature (Dipaolo and Tom 2009, Paik et al. 2011, Kim et al. 2016), but most of them have used small-scale physical models, and full-scale physical testing is rare.

In earlier articles (Paik et al. 2020a, 2020b), the authors conducted collapse tests on full-scale steel stiffened plate structures under axial-compressive loading at room temperature and cryogenic condition. In contrast to the case at room temperature triggered by ductile failure (buckling and plastic collapse), the structure tested at cryogenic condition is more prone to brittle fracture. The failure modes and ultimate strength of these structures have been discussed in detail in the authors' former works. The current study is a sequel to the earlier articles, where a temperature of -80°C is used as it is known as a transition temperature between ductile and brittle fracture (KSNA 1983, Kaminskji and Galatenko 1999, Tanguy et al. 2005a, Tanguy et al. 2005b, Nazari and Milani 2011, Nam et al. 2018, Tong et al. 2018, Perez-Martin et al. 2019).

The aim of the present paper is to develop full-scale collapse test data for steel stiffened plate structures at a temperature of -80°C, which will be useful to validate computational models for the ultimate strength analysis of steel plated structures at low temperatures. The paper also includes test data from room temperature to cryogenic condition. A material modelling approach is proposed how to represent a material's characteristics for different steel temperatures where ductility of material is predominant and no brittle fracture occurs.

2. Design and fabrication of the physical test structures

Three-bay stiffened plate structures were designed with two transverse frames and four longitudinal stiffeners as shown in Figure 1. The physical test structure (hereafter referred to as tested structure) was determined from outer bottom plate panels of an as-built 1900 TEU containership. Both transverse frames and longitudinal stiffeners had T-type as shown in Figure 2. The dimensions of the test structure were exactly the same as those described in Paik et al. (2020a, b). The thickness of plating was 10 mm.

The structure was fabricated in a shipyard in Busan, South Korea, using exactly the same technology of welding as used in today's shipbuilding industries. Figure 3 shows the fabrication of the tested structures in the shipyard. Details of the fabrication are referred to Paik et al. (2020a, b), while the welding-induced initial imperfections were measured and reported in Yi et al. (2020a, b).
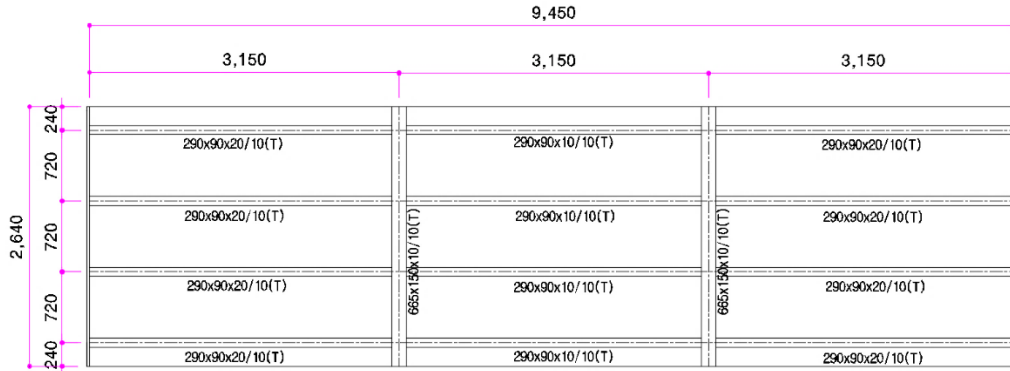
Figure 1. Dimensions of the full-scale steel stiffened plate structure (in mm).
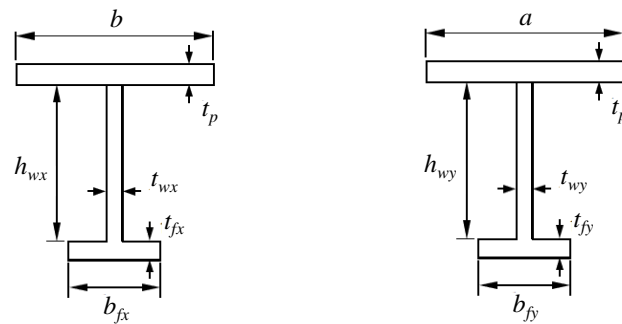
(a) Longitudinal stiffener   (b) Transverse frame

**Figure 2.** T-type of the longitudinal stiffener and transvers frame.

Figure 3. The fabrication of the tested structure at the shipyard.

3. Mechanical properties of AH32 steel in tension and compression at low temperatures

The tested structure was made of high tensile steel with grade AH32. Prior to the axial compression test of the structure, the mechanical properties of the material was

determined both in tension and in compression at different temperatures because the Bauschinger effect cannot be neglected at low temperatures (Paik 2018).
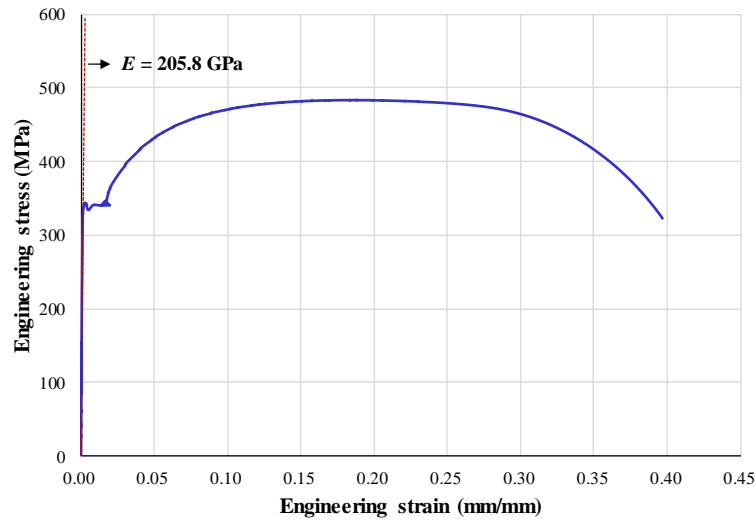
Figure 4. Engineering stress versus engineering strain curve of AH32 steel.

Figure 4 shows the engineering stress-engineering strain curve of AH32 steel at room temperature (20°C) obtained from tensile coupon tests. It is considered that at room temperature the mechanical properties of steel in tension are the same as those in compression where the Bauschinger effect is usually neglected until the yield strength is reached (Paik 2018). Table 1 presents the mechanical properties of the material at room temperature, and details of the tensile coupon tests applied in the study are referred to the Paik et al. (2020a, b).

Table 1. Mechanical properties of AH32 steel used for the tested structure at room temperature (20°C).

Elastic modulus, (GPa)	Yield strength, σ_Y (MPa)	Ultimate tensile strength, σ_T (MPa)	Ultimate fracture strain, ε_T	Fracture strain, ε_f
205.8	358.03	497.07	0.193	0.376

At low (sub-zero) temperatures, coupon type specimens were used in the tension tests similar to those at room temperature (ASTM E8/E8M 2015) as shown in Figure 5, while round bar type specimens were used in the compression tests (ASTM E9 2018) as shown in Figure 6. The hole in shoulder of coupon type specimen was made to securely grab the universal test machine without slipperyness. Liquefied nitrogen gases were used to lower the temperature until the target temperature value using a cooling chamber facilitated with a universal test machine as shown in Figure 7. The cooling rate was set to -5°C/min, followed by a soaking time of 30 min. when the
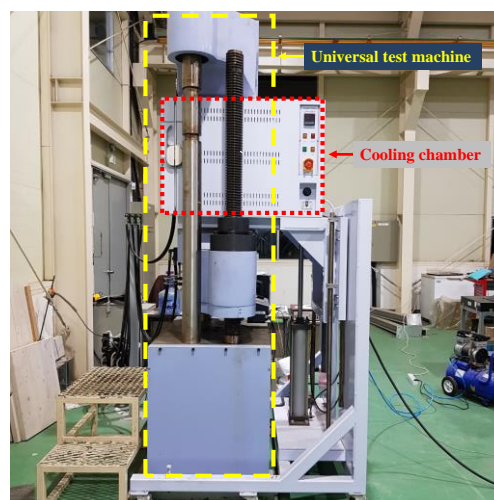
cooling was finished so that the target surface temperature was stabilized during the tests in accordance with ISO 6892-3 (ISO 2015); see Figure 8.
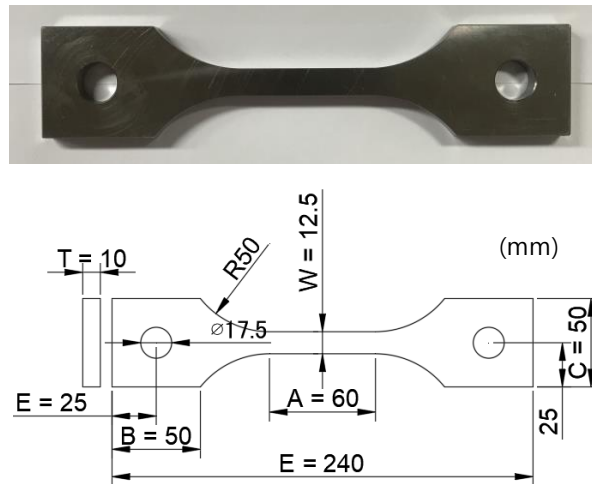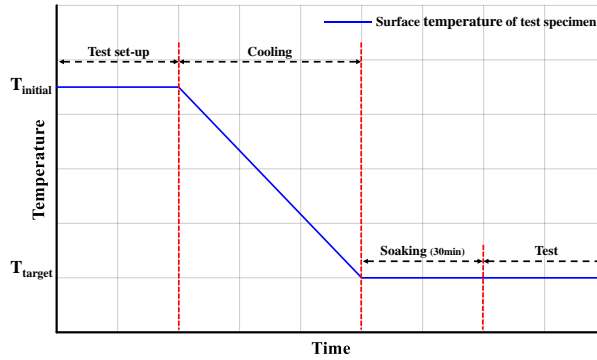

Figure 5. Test specimen used for the tension tests of the AH32 high tensile steel.
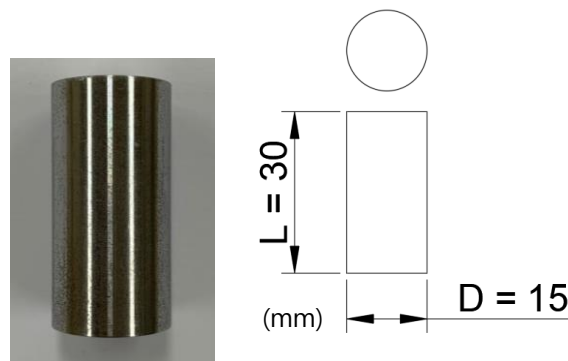
Figure 6. Test specimen used for the compression tests of the AH32 high tensile steel.


Figure 7. Universal test machine with a cooling chamber for the tension and compression tests at low temperatures.

Figure 8. Application of the soaking time to achieve stable conditions at low temperatures during the tests.

The tension and compression tests were conducted with different temperatures of the test specimens in a wide range of $20^{o}C$ (room temperature) to $-160^{o}C$ to look at an overall picture of material behaviour in association with the effects of low temperatures including the DBTT. The loading speed in the material tests (in either tension or compression) was 0.05 mm/s to achieve a quasi-static loading condition. A total of 36 tests were prepared to examine the low temperature effects on AH32 steel, where three specimens were tested at each temperature. Figure 9 shows the failure or deformed shapes of the tension test specimens at the different test temperatures. The fractured cross-sections of the specimens after the tests at different temperatures are also shown in Figure 9. Distinct differences of failure shapes in tension were not recognized in association with necking and failure (fracture). However, it is interesting to realize that the fractured cross-sections were quite different depending on the tested temperature. At room temperature, ductile fracture was dominant, and as the temperature was lowered, a more brittle fracture surface pattern with partial ductility appears in the temperature range $-40^{o}C$ to $-100^{o}C$. At temperature lower than $-100^{o}C$, the pattern of the fracture of surface was clearly brittle failure.

$20^{o}C$	$-40^{o}C$

-80$^{\mathrm{o}}$C	-100$^{\mathrm{o}}$C
-130$^{\mathrm{o}}$C	-160$^{\mathrm{o}}$C
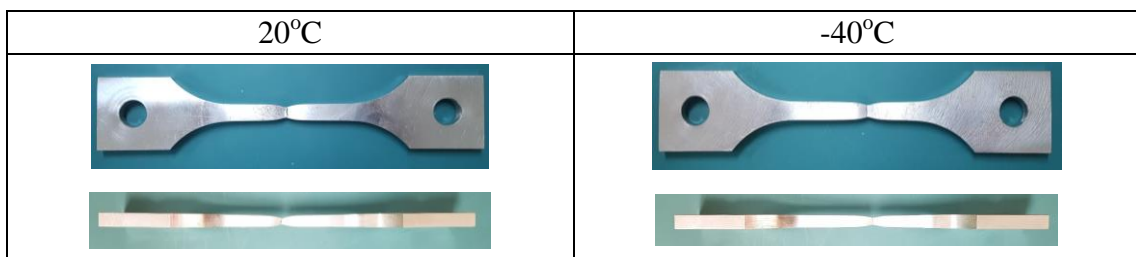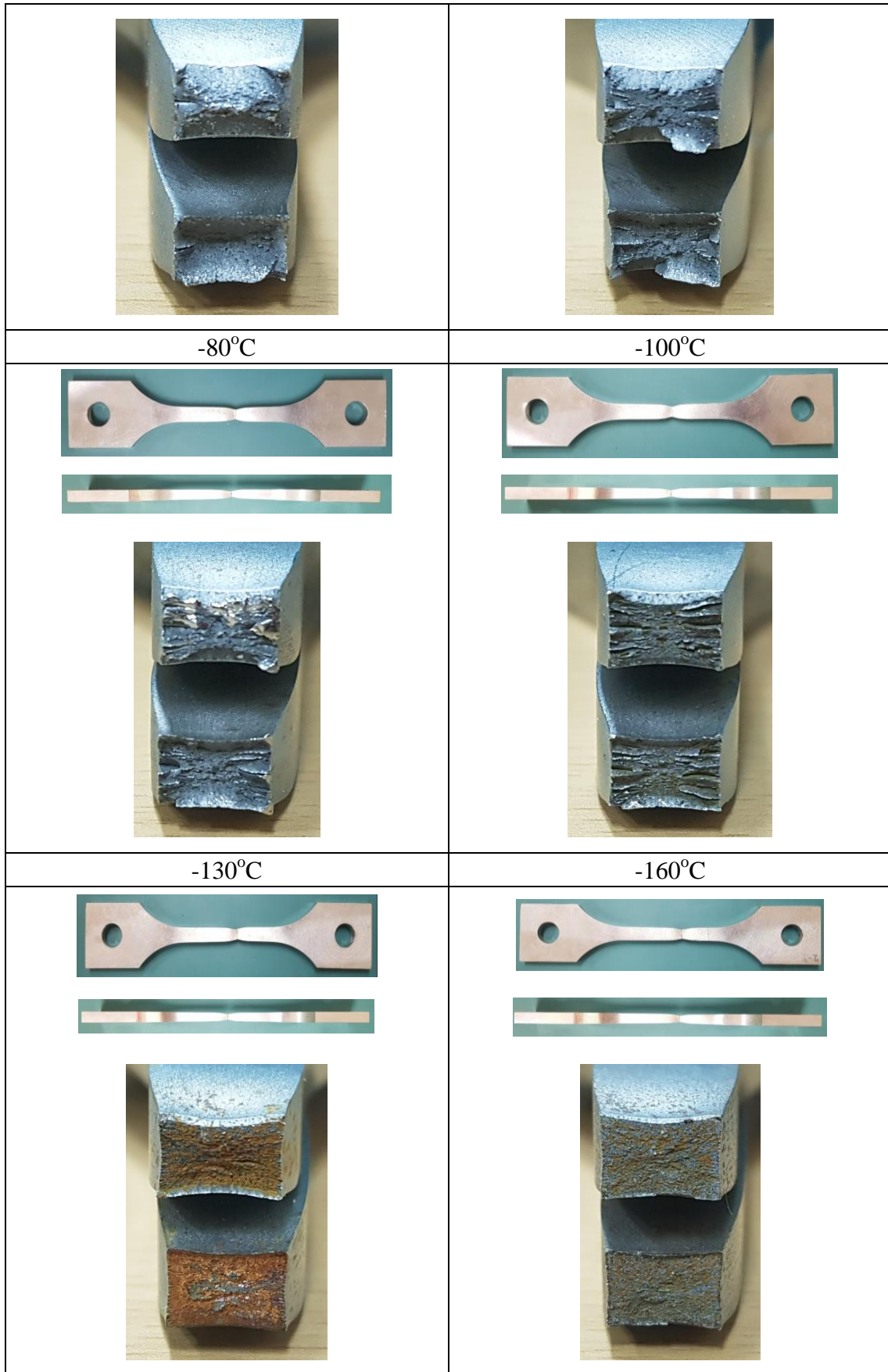
Figure 9. Failure shapes and fracture surfaces of the tension test specimens at different temperatures.
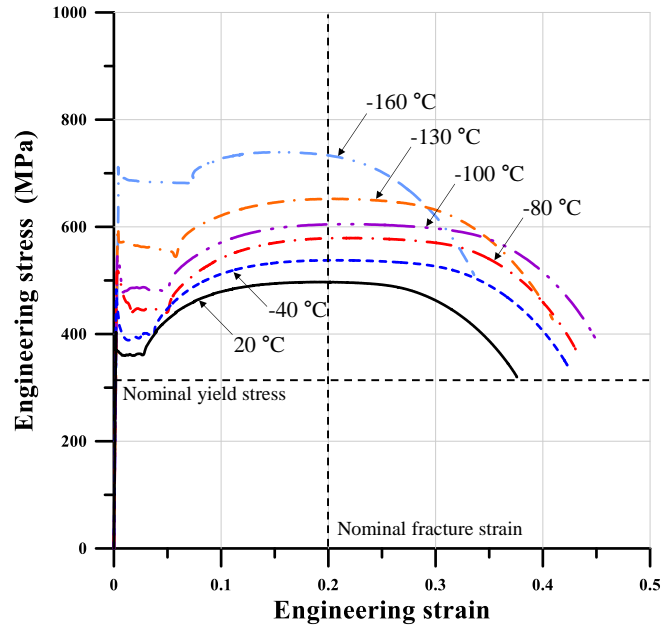
Figure 10 shows the obtained average engineering stress-engineering strain curves of AH32 steel at different temperatures and Table 2 summarizes the average mechanical properties. Figure 11 presents the variations of the average mechanical properties with temperature where each property has been normalized by its value at the reference (room) temperature. The results show that both the yield and ultimate tensile strengths increase as temperature decreases, and the former tends to increase faster than the latter. The elastic modulus obtained from the tension tests is unchanged despite the low temperature in contrast to that at elevated temperatures in fires (Paik 2018, 2019, Paik et al. 2020c, 2020d). The ultimate tensile strain or fracture (failure) strain increases until the temperature reaches -80°C, while it decreases for temperatures lower than -100°C.

Further material test studies are recommended, but it is considered based on the limited test database herein that the range of -80°C to -100°C is a transition temperature between ductile and brittle fracture in association with the fracture surfaces presented in Figure 9. This observation is similar to Majzoobi et al. (2016) who found that the transition from ductile to brittle failure of high tensile steels occur approximately at -80℃, and the material behaviour of steel is completely brittle at -196℃.

Table 2. Average mechanical properties of AH32 steel obtained from tension tests at different temperatures.

| Property	20℃	-40℃	-80℃	-100℃	-130℃	-160℃
Elastic modulus, E (GPa)	205.8	205.8	205.8	205.8	205.8	205.8
Yield strength, σ_Y (MPa)	358.03	391.02	433.48	472.52	546.74	672.96
Ultimate tensile strength, σ_T (MPa)	497.07	537.81	579.13	605.10	652.28	739.36
Ultimate tensile strain, ε_T	0.193	0.207	0.222	0.223	0.211	0.163
Fracture strain (-), ε_f	0.376	0.423	0.430	0.448	0.409	0.336

Figure 10. The average engineering stress-engineering strain curves in tension of AH32 steel at room and low temperatures.
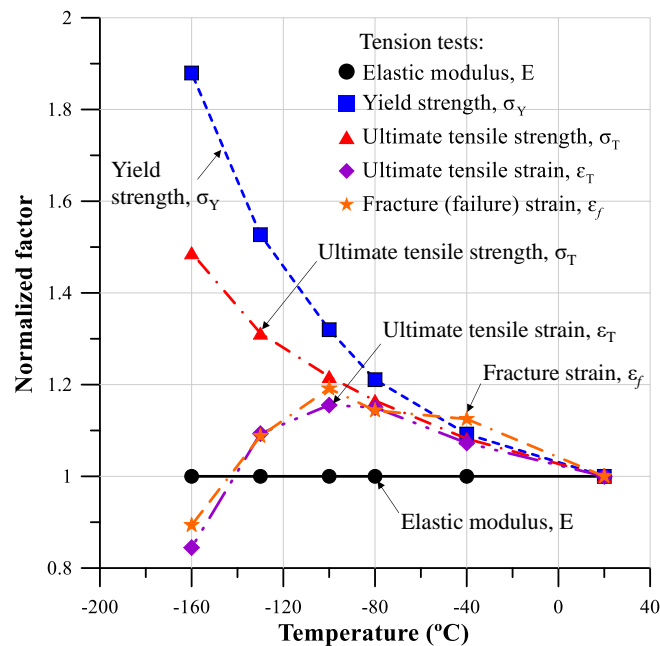

Figure 11. Presentation of normalised mechanical properties from tension tests at different temperatures for AH32 steel; see the text for details.

The deformed shapes of compression test specimens at different temperatures are presented in Figure 12. No distinct differences are seen in the deformed shapes of the test specimens after completion of the tests. Figure 13 presents the engineering stress-engineering strain results at the different temperatures, and the results confirm that there are only minor differences between the test temperatures. A comparison of the yield strengths in tension and in compression is presented in Figure 14. It shows

that the increase in yield strength when the temperature is decreased is much less moderate in compression compared to the tension tests. Table 3 summarizes the compression test results of the mechanical properties of AH32 steel. The elastic modulus of steel in compression is identical to that in tension. However, it is worth noting that the material behaviour in compression is totally different from that in tension after the yield strength is reached even at room temperature; compare the material behaviour in between Figures 10 and 13.

20^oC	-40^oC
-80^oC	-100^oC
-130^oC	-160^oC
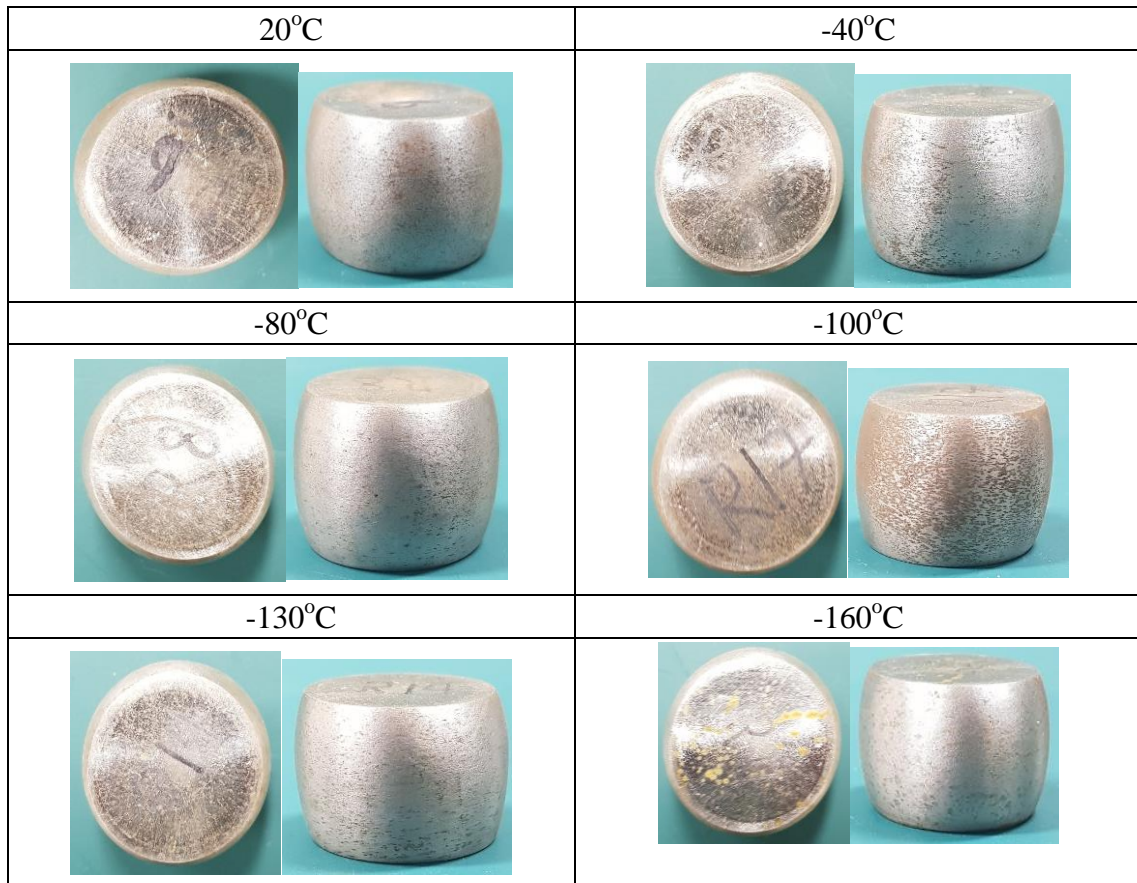
Figure 12. Deformed shapes of the compression test specimens at different temperatures.
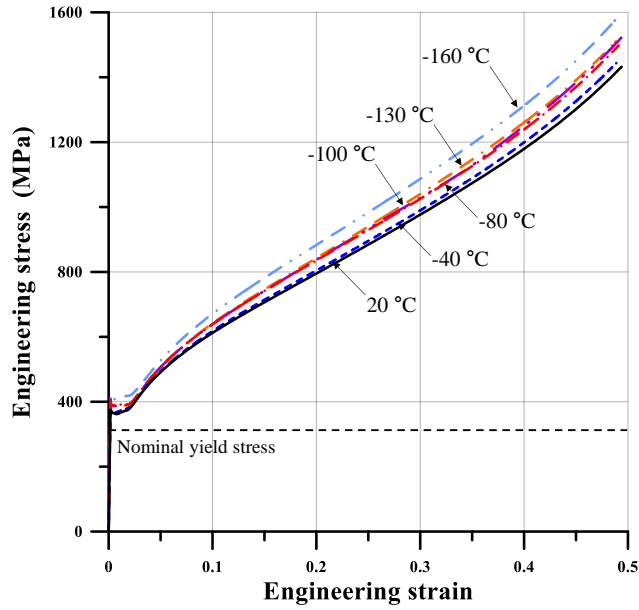
Figure 13. The average engineering stress-engineering strain curves in compression of AH32 steel at room and low temperatures.
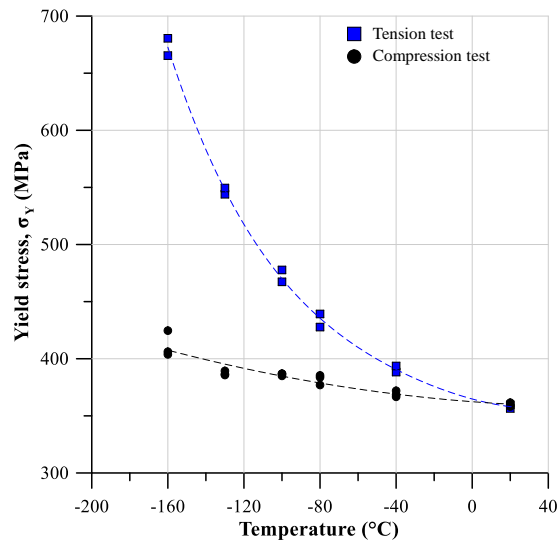
Figure 14. Comparison of yield strength between tension and compression for the AH32 high tensile steel at different temperatures.

Table 3. Average mechanical properties of AH32 steel obtained from compression tests at different temperatures.

Property	20°C	-40°C	-80°C	-100°C	-130°C	-160°C
Elastic modulus, E (GPa)	205.8	205.8	205.8	205.8	205.8	205.8
Yield strength, σ_Y (MPa)	359.65	369.06	382.01	386.22	387.20	411.51

4. Procedure for the full-scale collapse test of the steel stiffened plate structure

The full-scale test of the steel stiffened plate structure was carried out at the Korea Ship and Offshore Research Institute (KOSORI) test site in Hadong, South Korea (www.icass.center). Figure 15 shows the test set-up positioned at the test facility with jigs. The procedure of the test was exactly the same as those at room temperature and cryogenic condition presented in Paik et al. (2020a, b), although the current test focused on a temperature of -80°C. This low temperature was achieved by pouring liquefied nitrogen gases at the central bay of the tested structure and evaporated as shown in Figure 16. Polystyrene foam panels were used to house the liquefied nitrogen gases during the cooling period as shown in Figure 17 and removed as the target temperature was achieved.

One end of the test frame was fixed at a reaction wall, while the other end was subjected to axial compressive loads using two hydraulic actuators as shown in Figure 18. Each hydraulic actuator can carry up to 1,000 tonnes and the loading speed was kept at 0.25 mm/s which is considered to be a quasi-static loading condition. Other details of the test set-up and procedure are referred to in the earlier articles by Paik et al. (2020a, b).

Figure 15. The test set-up of the structure with jigs at the KOSORI test site.

Figure 16. Pouring of nitrogen gas at the central bay of the tested structure.
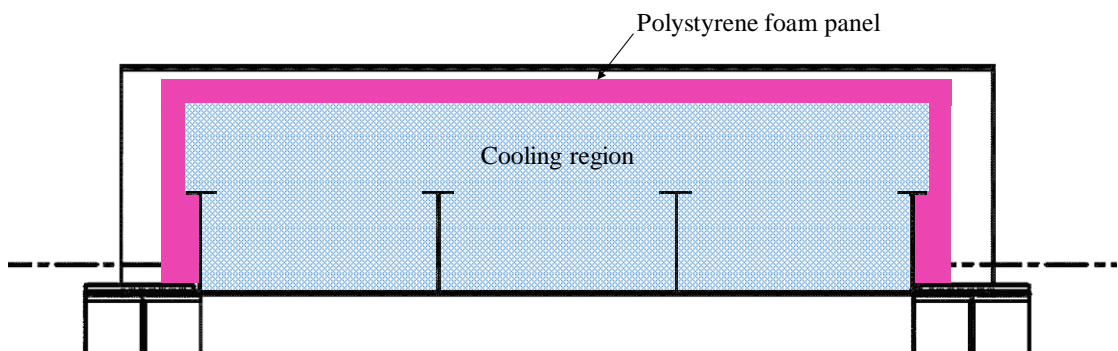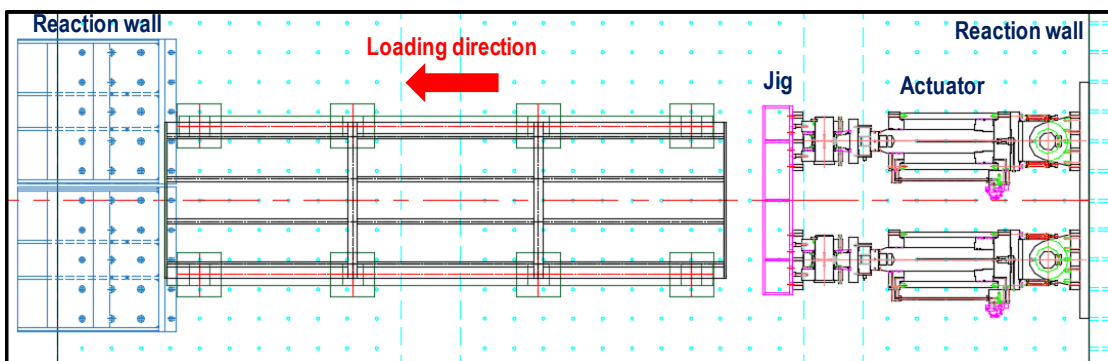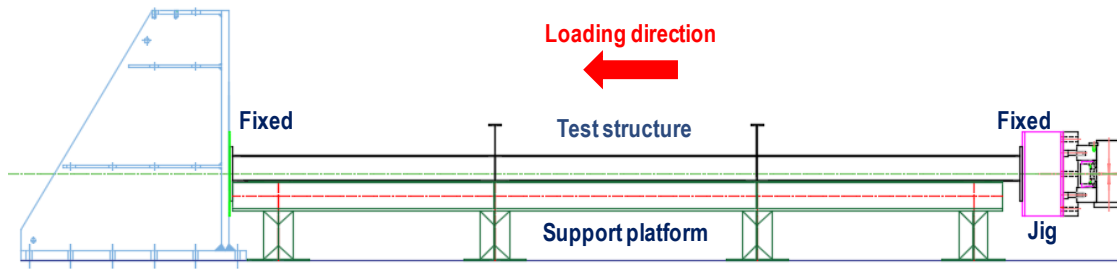

Figure 17. Illustration of housing of the cooling region by polystyrene foam panels.

(a) Plan view of the test set-up.

(b) Profile view of the test set-up.

Figure 18. Schematics of the test set-up.

5. Test results and discussion

5.1 Steel temperatures

The surface temperatures of the tested structure were measured using T-type thermocouples which were located outside the cooling region to minimize the effect of cold air during and after evaporation of the released nitrogen gases. Figure 19 shows the results from the temperature measurements at different locations, and Table 4 presents the results of the maximum and minimum temperatures measured in these monitoring points. The average temperatures are also indicated in Table 4. It is found that the average temperature was -83.2℃ in the plating, -78.3^{o}C in the longitudinal stiffener's web, and -73.5℃ in the longitudinal stiffener's flange.
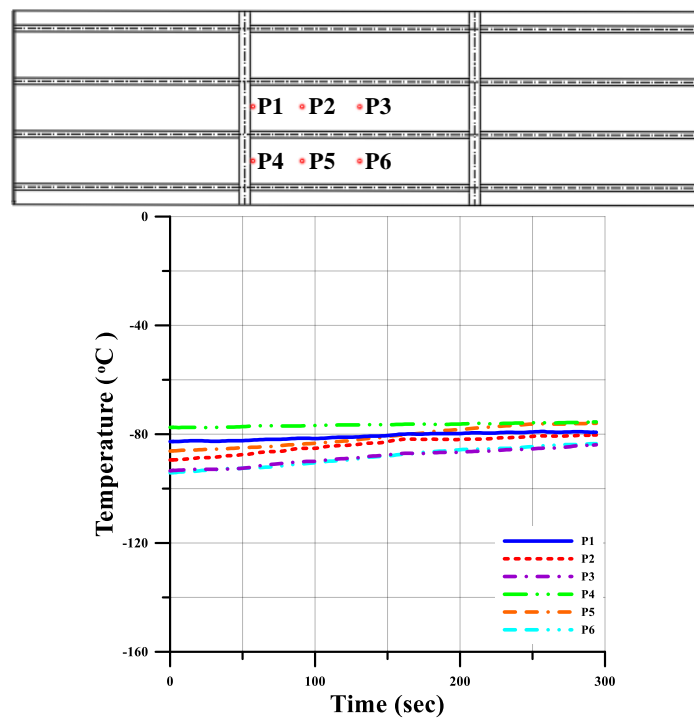
(a) Measured temperature in the plating.
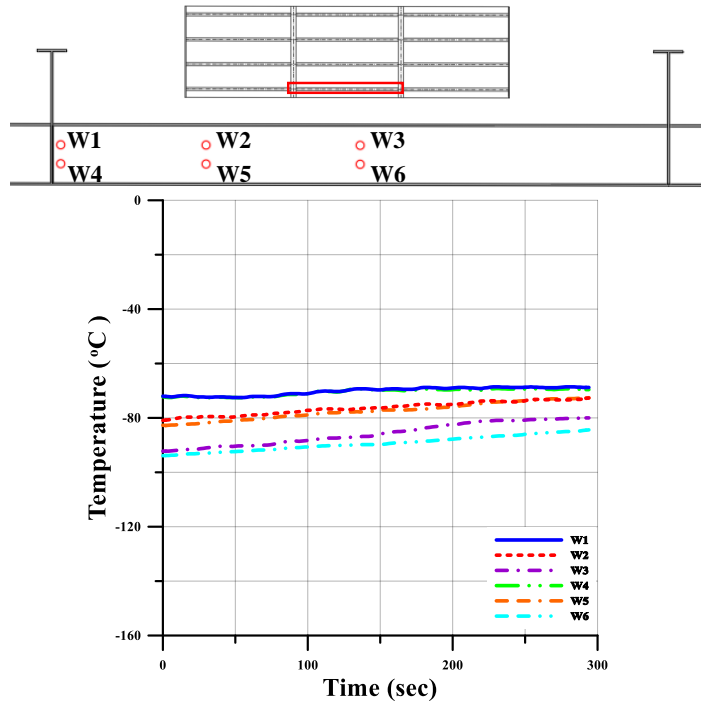
(b) Measured temperature in the longitudinal stiffener's web.
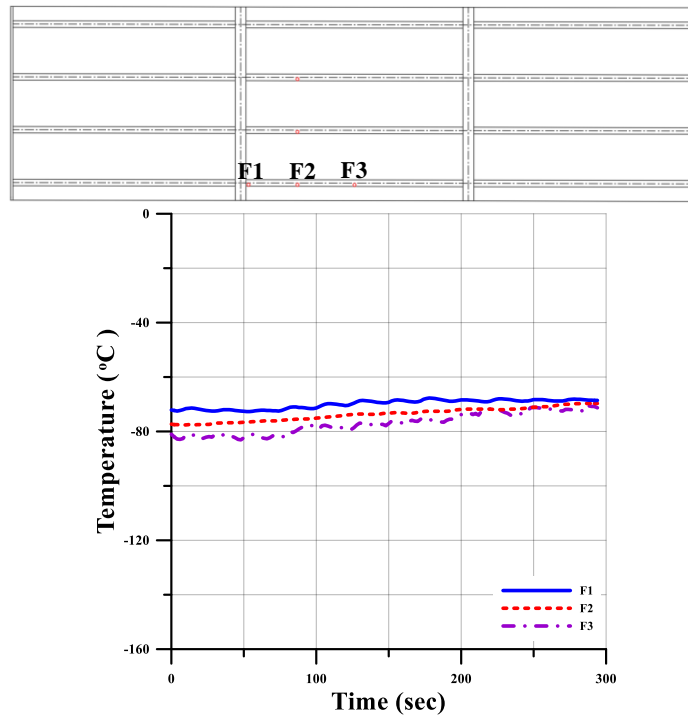
(c) Measured temperature in the longitudinal stiffener's flange.

Figure 19. Measured temperatures in the steel during 300 seconds in different locations.

Table 4. Measured steel temperatures after 300 seconds.

Location		Maximum temperature (℃)	Minimum temperature (℃)	Average temperature (℃)	Average temperature in overall (℃)
Plating	P1	-79.0	-82.7	-80.7	
	P2	-80.9	-89.5	-83.8	
	P3	-83.9	-93.5	-88.5	-83.2
	P4	-75.5	-77.6	-76.5	
	P5	-76.0	-86.2	-80.9	
	P6	-83.5	-94.2	-88.4	
Longitudinal stiffener web	W1	-68.6	-72.5	-70.2	
	W2	-72.7	-80.9	-76.4	
	W3	-80.0	-92.2	-85.7	-78.3
	W4	-69.2	-72.6	-70.5	
	W5	-72.6	-82.8	-77.5	
	W6	-84.4	-93.9	-89.4	
Longitudinal stiffener flange	F1	-67.7	-72.7	-69.9-	
	F2	-69.7	-77.6	-73.7	-73.5
	F3	-70.6	-83.1	-77.0	

5.2 Collapse behavior

The Appendix presents the test data of the ultimate strength behavior of the tested structure at -80°C in terms of the axial compressive load versus the axial shortening relation. Figure 20 shows the deformed shapes of the test structure after the ultimate strength was reached. It is seen in Figure 20 that flexural-torsional buckling (or tripping) of the stiffener triggered the structural collapse but no brittle fracture happened in contrast to the structure tested at cryogenic condition which reached the ultimate strength triggered by brittle fracture (Paik et al. 2020b).

(a) Initial status (before compressive loading).

(b) Status after reaching the ultimate strength at the temperature -80℃.

Figure 20. Geometrical status of the tested structure at the temperature -80℃.

Figure 21 compares the ultimate strength behavior of the tested structure at -80°C with that at 20°C (Paik et al. 2020a) and -160°C (Paik et al. 2020b). The ultimate strength of the structure tested at -80°C is 11.63% larger than for the room temperature case, which is related to the fact that the yield strength of the material at -80°C is larger than the yield strength at room temperature; see section 3. It should be noted that the tested structures at 20°C and -80°C showed ductile failure associated to buckling and plastic collapse and tripping of the stiffener triggered the collapse of these structures. However, the structure tested at cryogenic condition (-160°C) reached the ultimate compressive strength triggered by brittle fracture, and its ultimate strength value was larger than for the structure tested at 20°C but lower than the structure tested at -80°C. It can be explained because the brittle fracture caused a sharp drop of internal forces (falling in catastrophic instability of the structure) after the ultimate strength was reached.

Table 5 summarizes the ultimate compressive strength behaviours of the three test cases. It is noted that the differences of the ultimate strength behaviour are due to various sources of uncertainties involved in individual structures tested at different temperatures. However, it is obvious that testing full-scale structures is one of the benefits to capture nonlinear physics in association with multiple scales and multiple criteria. Furthermore, fabrication-related uncertainties were minimized using exactly the same technology of welding as used in today's shipbuilding industries.

17
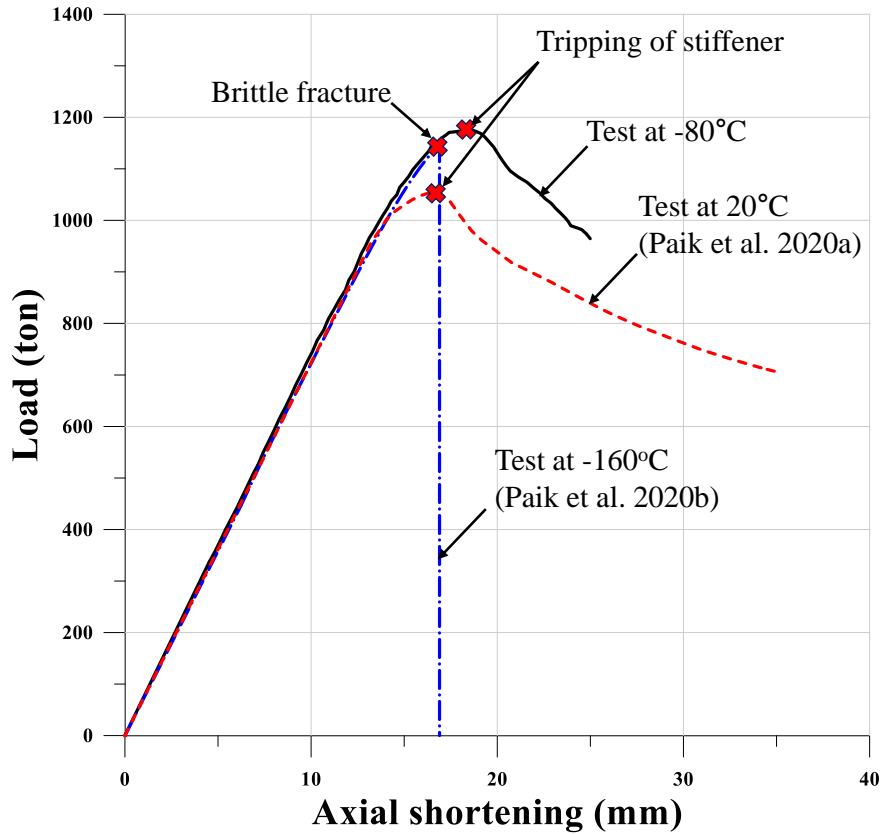
Figure 21. Comparison of the ultimate compressive strength behaviour for the three structures tested at the temperatures 20°C, -80°C and -160°C.

Table 5. Comparison of the ultimate compressive strength for the three structures tested at three different temperatures.

| Property	20℃ (Paik et al. 2020a)	-160°C (Paik et al. 2020b)	-80℃ (Present)
Stiffness (ton/mm)	72.36	72.38 (+ 0.03%)	72.12 (- 0.33%)
Ultimate strength (ton)	1054.04	1149.06 (+ 9.02%)	1176.58 (+11.63%)
Axial shortening up to collapse (mm)	16.40	16.90 (+ 3.05%)	18.46 (+ 12.56%)
Strain energy up to collapse (ton·mm)	9506.43	10179.96 (+ 7.09%)	12224.60 (+ 28.59%)
Local buckling	Tripping of stiffener	None	Tripping of stiffener
Fracture type	None	Brittle fracture	None

Note: The values within the parenthesis indicate a ratio to the reference value at 20℃.

6. Nonlinear finite element method analyses

Nonlinear finite element method (NLFEM) analyses were performed to predict the ultimate strength behaviour of the tested structures at 20°C; see Lee and Paik (2020) and at -160°C; see Lee et al. (2020). In the present paper, the ultimate compressive strength of the tested structure at -80°C was computed using the LS-DYNA implicit solver (LS-DYNA 2019). ALPS/ULSAP (2020), the ultimate strength analysis program for plates and stiffened panels, was also used to predict the ultimate compressive strength for a comparison.

6.1 Finite element mesh modelling

The FE mesh was designed using only 4-node shell elements (with the fully-integrated shell element formulation 16 in LS-DYNA implicit code) for the plating, the stiffeners and the transvers frames. A convergence analysis to define the best mesh size for the tested structure involving local buckling and plasticity was carried out varying mesh sizes, and it was found that a mesh size of 40 mm $\times$ 40 mm could be adopted; see Figure 22 which shows the FE model of the tested structure.
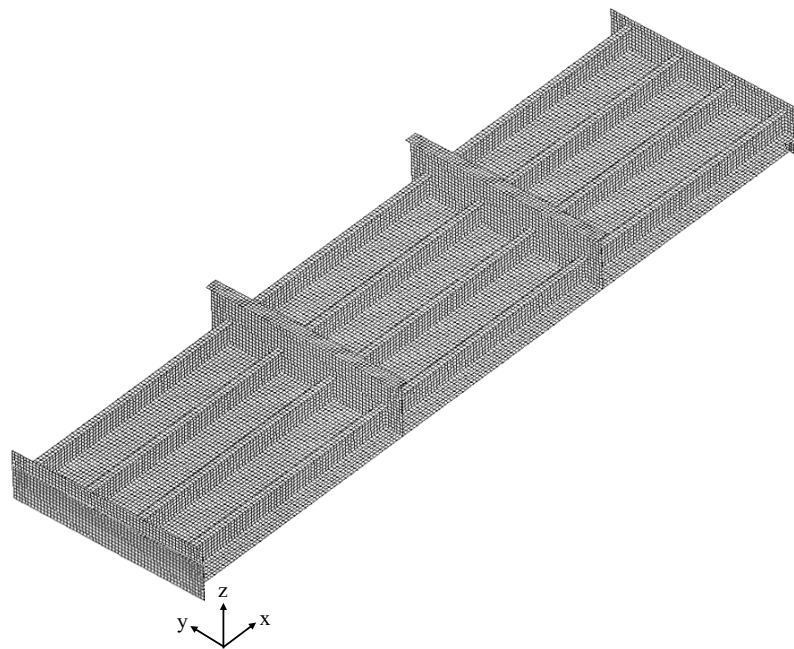

Figure 22. Finite element mesh model of the tested structure.

6.2 Loading and boundary conditions

The compressive loads were applied using a displacement control method similar to how the load was applied in the physical test where the loaded edge was kept straight. The loading speed was set to be in a quasi-static condition at 0.25 mm/s in accordance with the physical testing.

Figure 23 shows the boundary conditions applied on the FE model. One end of the tested structure was fixed at the reaction wall. The loaded edge was coupled to acquire a condition of a uniform and straight line. The unloaded edges (both sides of the tested structure) were free except for vertical deformation which was constrained as the tested structure was supported by rigid jigs along the unloaded edges; see Figures 17 and 18.
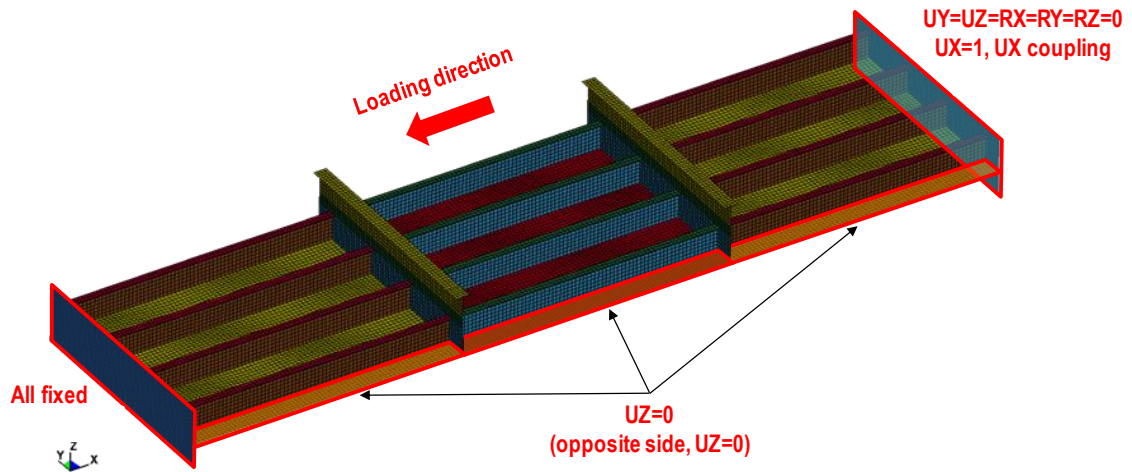
Figure 23. The loading and boundary conditions of the FE model.

Table 6. Material properties of AH32 steel used in the FE model

Property	20°C		-80°C	
	Tension	Compression	Tension	Compression
Elastic modulus, E (GPa)	205.8	205.8	205.8	205.8
Yield strength, σ_Y (MPa)	358.03	359.65	433.48	382.01
Fracture strain, ε_{ft}	0.376	-	0.430	-
Poisson's ratio	0.3	0.3	0.3	0.3

6.3 Material property modelling

Among LS-DYNA material cards, *MAT124 was used for representing the material properties in tension and in compression at 20°C and -80°C as listed in Table 6. This is an elastic-perfectly plastic material model but with different properties in tension and in compression depending on low temperatures. Figure 24 shows the idealized relation of the engineering stress versus engineering strain used for the ultimate compressive strength analysis in which ductility of material is predominant and no brittle fracture occurs. Only the middle bay of the tested structure was exposed to -80°C, while the outer two bays were always at room temperature.
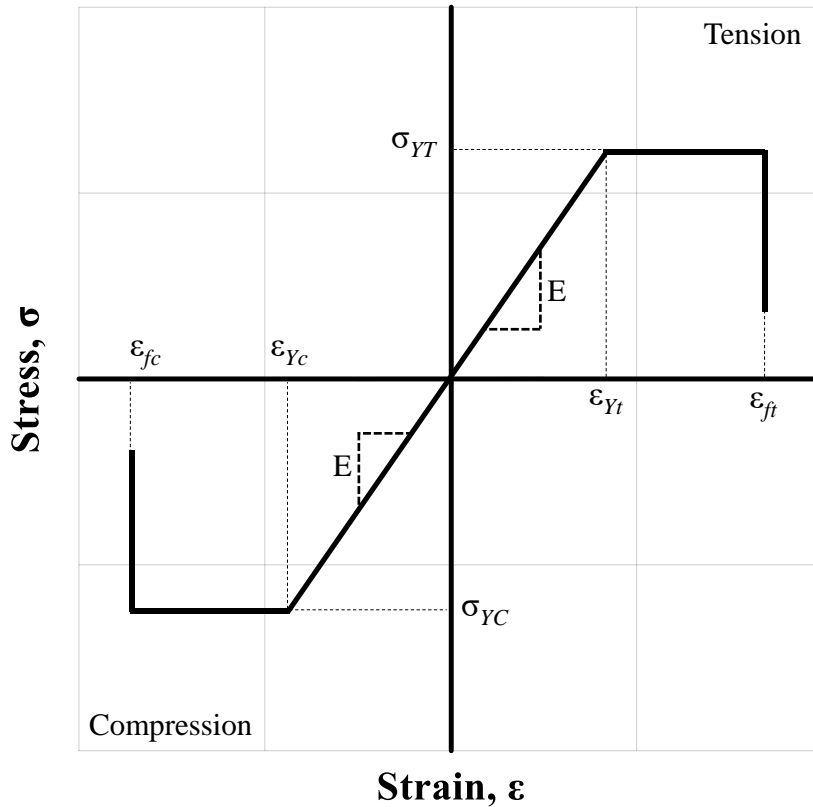
Figure 24. Idealized stress-strain relation used for the ultimate compressive strength analysis.

6.4 Welding-induced initial deformations

Yi et al. (2020a) measured the welding-induced initial deformations of the tested structure which comprise three components, namely local plate initial deflection, column type initial deflection of stiffener and sideways initial deflection of stiffener, as shown in Figure 25 (Paik 2018). Figure 26 shows the measured and idealized deformations of the tested structure due to fabrication by welding. It is seen from Figure 26 that the two transverse frames also deformed, and the initial deflection pattern of plating between the transverse frames is the so-called hungry horse's back shape. In the present study, the direct measurements were used, but some idealization of measured data was made to present a continuous shape of initial deformation which was easier to prepare the input data for the LS-DYNA ultimate strength analysis.
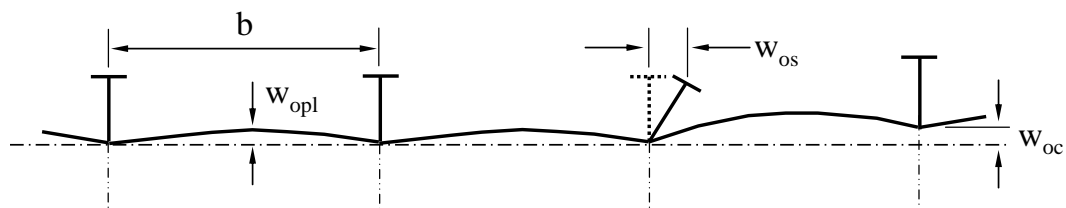
Figure 25. Three types of welding-induced initial deformations in a stiffened plate structure.
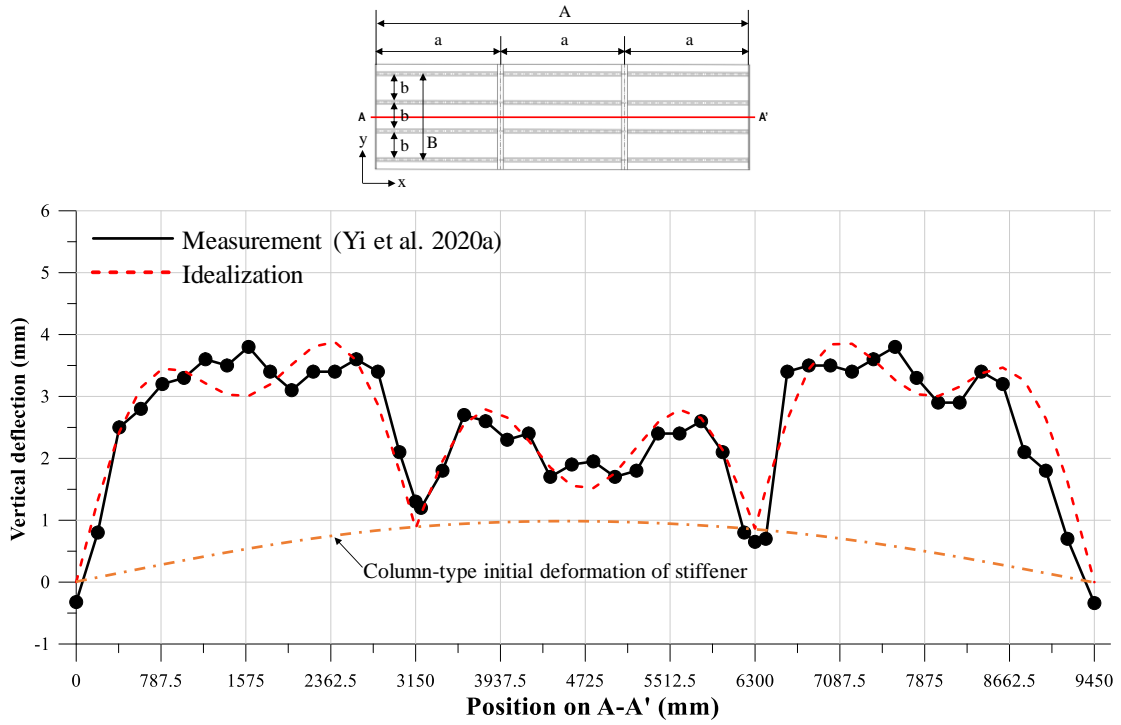
Figure 26. Measured and idealized deformations of the tested structure due to fabrication by welding.

As such, Equations (1) to (3) were approximately formulated to present the three types of welding-induced initial deformations. Figure 27 shows the finite element model including welding-induced initial deformations in the tested structure.

Initial deflection of plating:

$$w_{opl} = w_{opl}^* + w_{opl}^{**} \tag{1.a}$$

$$w_{opl}^* = w_{o\max} \sin\frac{m\pi x}{a}\left|\sin\frac{n\pi y}{b}\right| \quad \text{with } m=1,\ n=1,\ w_{o\max} = \begin{cases} 3.5 & for\ 0 \le x \le a,\ 2a \le x \le 3a \\ 1.5 & for\ a \le x \le 2a \end{cases}$$

$$\tag{1.b}$$

$$w_{opl}^{**} = w_{o\max} \sin\frac{m\pi x}{a}\left|\sin\frac{n\pi y}{b}\right| \quad \text{with } w_{o\max} = 1.0,\ m=3,\ n=1 \tag{1.c}$$

Column-type initial deformation of stiffener (over the entire length of the structure):

$$w_{oc} = w_{oc\max} \sin\frac{m\pi x}{A} \sin\frac{n\pi y}{B} \quad \text{with } w_{oc\max} = 1.0,\ m=1,\ n=1 \tag{2}$$

Sideways initial deformation of stiffener:

$$w_{os} = w_{os\max} \frac{z}{h_w} \sin\frac{\pi x}{a} \quad \text{with } w_{os\max} = 0.000133a \tag{3}$$

22

where z is the coordinate in the direction of stiffener web height, and h_w is the stiffener web height.
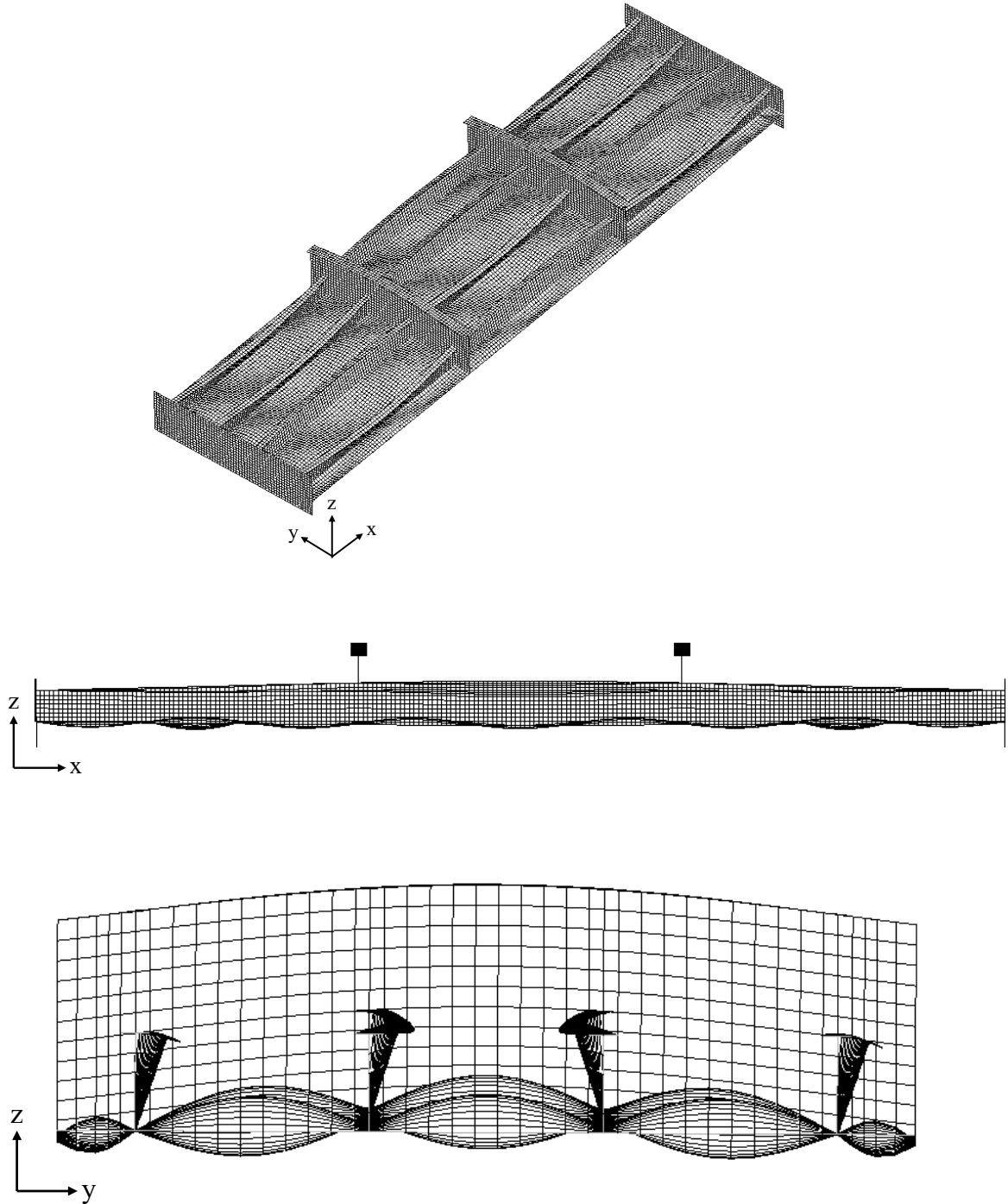
Figure 27. Welding-induced initial deformations applied to the FE model (with an amplification factor of 100 for plating and column-type, and 20 for sideways initial deformations).

6.5 Welding-induced residual stresses

As the welding was conducted in both the longitudinal and the transverse directions to attach the longitudinal stiffeners and the transverse frames, biaxial residual stresses developed (Paik 2018). As per Yi et al. (2020b), direct measurements of residual stresses in the plating between the support members were applied but with some idealization for the ultimate compressive strength analysis. Figure 28 presents the idealized distribution of the biaxial residual stresses in the plating. Table 7 presents the properties of the residual stresses, where σ_{rtx} is the tensile residual stress in the x-direction and σ_{rty} is tensile residual stress in the y-direction. The stresses σ_{rcx} and σ_{rcy} are the compressive residual stress in the x- and y-directions, respectively, and a_t and b_t are the breadth or length of the related tensile residual stress regions (Paik 2018).
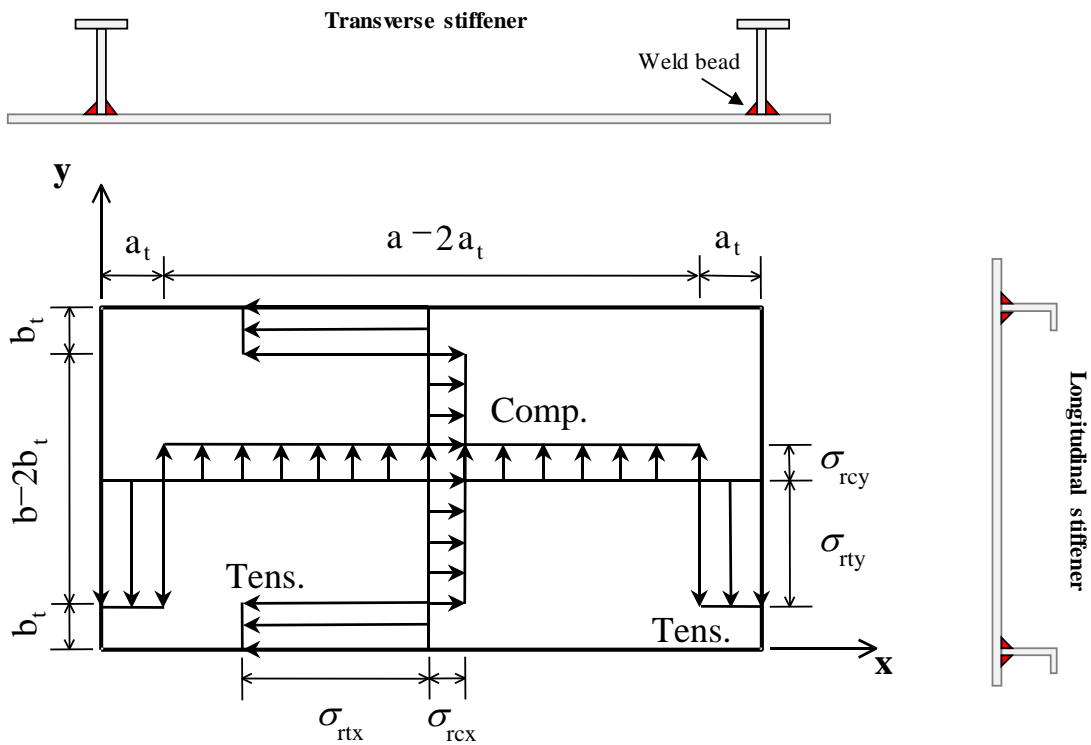
Figure 28. Idealized distribution of biaxial residual stresses in plating of the tested structure.

Table 7. Properties of the residual stresses in the plating of the tested structure.

| Property	Transverse direction	Property	Longitudinal direction
b_t	39.61 mm	a_t	51.47 mm
σ_{rcx}	-0.110 σ_{YT}	σ_{rcy}	-0.030 σ_{YT}
σ_{rtx}	+0.90 σ_{YT}	σ_{rty}	+0.90 σ_{YT}

6.6 Computed results and discussion

Figure 29 and Table 8 compare the computed results using the FE model with the measured data from the test. The predictions of ALPS/ULSAP (2020) are also compared, where the details of ALPS/ULSAP (2020) modeling are referred to in Lee and Paik (2020). The yield strength of 382.01 MPa by material test in compression was used for the ultimate strength calculation for -80°C, while the tensile yield strength was used for 20°C as it is almost identical to the compressive yield strength. For a comparison, the ultimate strength with a yield strength of material obtained from tension test was also calculated at -80°C as indicated in Table 8.

The ultimate strength of the structure tested at -80°C is 11.63% greater than for the structure tested at room temperature. For the temperature of -80°C, the NLFEM overestimates the ultimate compressive strength behavior compared to the experimental results by 8.7% in the peak load. Other properties are also compared in Table 8. Figure 30 compares the deformed shape of the tested structure between the FE analysis and the experiment after the ultimate strength was reached, where the collapse pattern is similar with tripping of stiffener. Predictions of ALPS/ULSAP in the ultimate compressive strength at both 20°C and -80°C are in good agreement with test results. Also, ALPS/ULSAP predicted the same collapse mode (tripping of stiffener) as the tests. It is concluded that NLFEM and ALPS/ULSAP are useful to compute the ultimate strength behavior at low temperatures as long as brittle fracture does not happen.
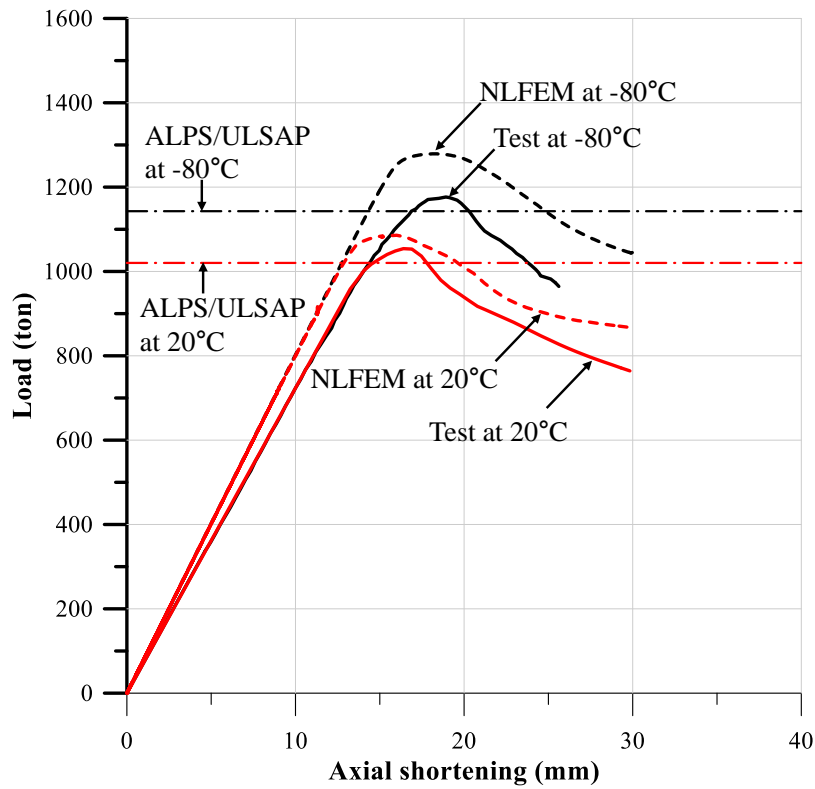
(a) Load versus axial shortening
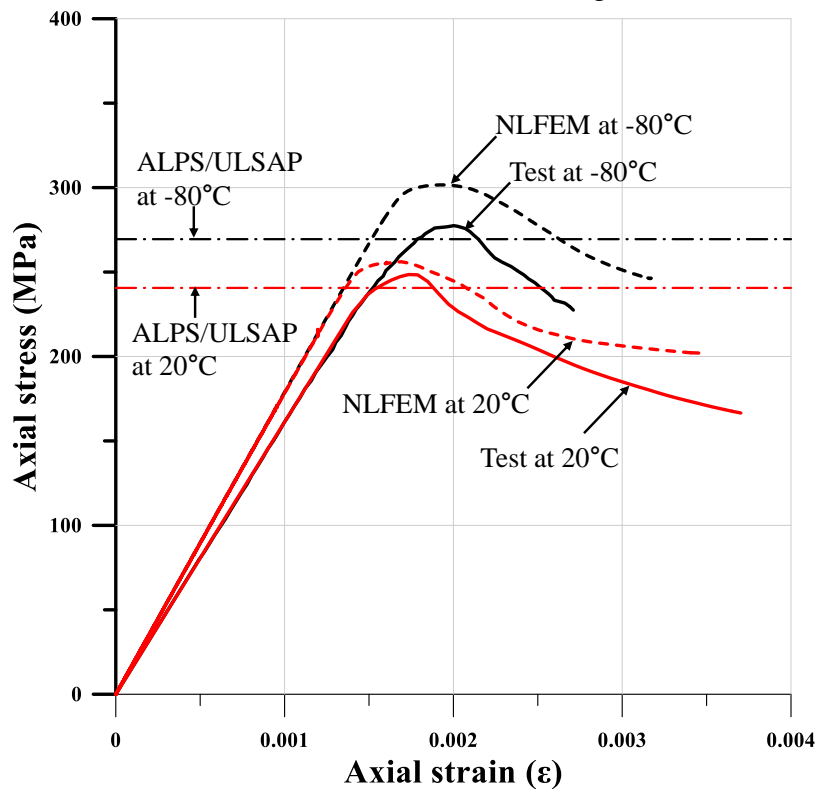
(b) Axial stress versus axial strain

Figure 29. Comparison of the ultimate strength behaviour of the test structure between the FE analysis and the experiment at the test temperature -80$^{\text{o}}$C.

Table 8. Comparison of the ultimate compressive strength behaviour between test, NLFEM and ALPS/ULSAP.

Parameter	Test		NLFEM		ALPS/ULSAP	
	20°C	-80°C	20°C	-80°C	20°C	-80°C
Stiffness (ton/mm)	72.16	72.12	80.82	80.82	-	-
Ultimate compressive load (ton)	1054.04	1176.58	1085.97	1278.95	1020.28	1142.83[1] / 1266.66[2]
Ultimate compressive stress (MPa)	248.56	277.45	256.09	301.60	240.60	269.501[1] / 298.70[2]
Axial shortening up to collapse (mm)	16.40	18.46	16.00	18.22	-	-
Strain energy up to collapse (ton·mm)	9560.43	12224.60	10169.04	13070.89	-	-
Local buckling	Tripping	Tripping	Tripping	Tripping	Tripping	Tripping
Brittle fracture	None	None	None	None	None	None

Note: 1) The compressive yield strength of 382.01 MPa was used. 2) The tensile yield strength of 433.48 MPa was used.
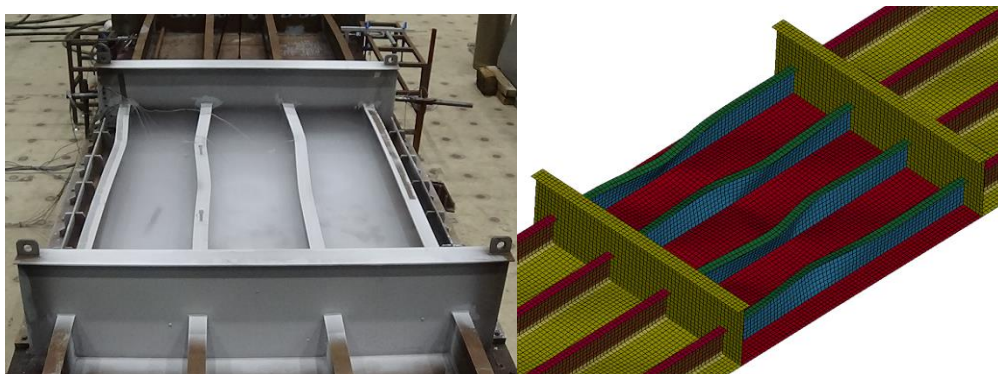
Figure 30. Comparison of the deformed shape of the tested structure between test and NLFEM after reaching the ultimate strength at -80°C.

7. Concluding remarks and further studies

The aim of the present study was to develop a test database on the ultimate strength of a full-scale steel stiffened plate structure subjected to an axial-compressive load and a temperature of -80°C. Based on the study, the following conclusions can be drawn.

1. The tested structure was made of AH32 steel. The mechanical properties of the material were obtained from tension and compression tests that were conducted at the temperatures 20°C, -40°C, -80°C, -100°C, -130°C and -160°C. The results from the material tests confirmed that the Bauschinger effect cannot be neglected at low temperatures in contrast to the case at room temperature. Also, it is observed that the temperature range -80°C to -100°C is a transition region between ductile and brittle fractures of the high tensile steel, but further investigations are recommended on this topic.

2. The dimensions of the tested structure were the same as those tested in the former works by the authors; see Paik et al. (2020a, b). The tested structure was fabricated at a shipyard using exactly the same technology of welding as used in today's shipbuilding industry to minimize fabrication-related uncertainties. The welding-induced initial deformations and the residual stresses were measured and presented in Yi et al. (2020a, b).

3. The tested structure was cooled down to -80°C and subjected to axial-compression loading. It reached its ultimate strength by tripping (lateral-torsional buckling) of the stiffeners after buckling and plastic collapse of plating, which was similar to the collapse pattern observed for a structure tested at room temperature (Paik et al. 2020a). No brittle fracture happened at -80°C nor at 20°C in contrast to at the cryogenic condition (-160°C) where the ultimate strength of the tested structure was triggered by brittle fracture (Paik et al. 2020b). The ultimate strength of the structure tested at -80°C was 11.63% greater than for the structure tested at room temperature. This is primarily due to the fact that the yield strength of the material at -80°C is larger than that at room temperature.

4. A nonlinear FE model was designed to account for the material's Bauschinger effect obtained from the results from the tension and compression material tests, and the actual steel temperatures measured during the experiment of the structure. It is found that nonlinear FE analysis with the material model based on the material test data is able to capture the ultimate compressive strength behaviour of supersized structures at low temperatures as far as the material properties together with steel temperatures of the structures are defined correctly where ductility of material is dominant and no brittle fracture occurs. It is recommended to formulate a similar material model which accounts for the ductile-to-brittle fracture transition and entire brittle-fracture.

5. The test data obtained from the present study can be used to validate computational models for the ultimate compressive strength analysis of steel stiffened plate structures at low temperatures which do not show brittle fracture.

Acknowledgements

ORCID

Jeom Kee Paik: http://orcid.org/0000-0003-2956-9359
Dong Hun Lee: https://orcid.org/0000-0003-2829-0719
Dae Kyeom Park: https://orcid.org/0000-0002-9833-0352
Jonas W. Ringsberg: http://orcid.org/0000-0001-6950-1864

References

ALPS/ULSAP. 2020. Ultimate strength analysis of plates and stiffened panels under combined biaxial compression / tension, edge shear and lateral loads. MAESTRO Marine LLC, Greenboro, MD, USA.

ASTM. 2015. E8/E8M: Standard test methods for tension testing of metallic materials. ASTM International.

ASTM. 2018. E9: Standard test methods of compression testing of metallic materials at room temperature. ASTM International.

Dipaolo BP, Tom JG. 2009. Effects of ambient temperature on a quasi-static axial-crush configuration response of thin-wall, steel box components. Thin-Wall Structures, 47: 984-997.

Hughes OF, Paik JK. 2013. Ship structural analysis and design. Alexandria, USA: The Society of Naval Architects and Marine Engineers.

ISO. 2015. 6892-3: Metallic materials — Tensile testing at low temperature — Part 3: Method of test at low temperature. International Organization for Standardization, Switzerland.

Kaminskji AA, Galatenko GV. 1999. On the temperature dependence fracture toughness in the brittle-to-ductile transition region. International Applied Mechanics. 35(4): 398-404.

Kim KJ, Lee JH, Park DK, Jung BK, Han X, Paik JK. 2016. An experimental and numerical study on nonlinear impact responses of steel-plated structures in an Arctic environment. International Journal of Impact Engineering. 93: 99-115.

KSNA. 1983. Handbook for ship design. 4th Edition, The Kansai Society of Naval Architects, Osaka, Japan (in Japanese).

Lee HH, Paik JK. 2020. Ultimate compressive strength computational modelling for stiffened plate panels with non-uniform thickness. Journal of Marine Science and Application, Submitted for publication.

Lee DH, Ringsberg JW, Tan PJ, Paik JK. 2020. A practical technique for the ultimate compressive strength analysis of steel stiffened plate structures triggered by brittle fracture at cryogenic condition. The Korea Ship and Offshore Research Institute (The International Centre for Advanced Safety Studies), Pusan National University, Busan, South Korea.

LS-DYNA. 2019. LS-DYNA user's manual. Livermore Software Technology Corporation, Livermore, CA, USA.

Majzoobi GH, Mahmoudi AH, Moradi S. 2016. Ductile to brittle failure transition of HSLA-100 steel at high strain rates and subzero temperatures. Engineering Fracture Mechanics. 158: 179-193.

Nam W, Hopperstad OS, Amdahl J. 2018. Modelling of the ductile-brittle fracture transition in steel structures with large shell elements: A numerical study. Marine Structures. 62: 40-59.

Nazari A, Milani AA. 2011. Ductile to brittle transition temperature of functionally graded steels with crack arrester configuration. Materials Science and Engineering: A. 528(10-11): 3854-3859.

Paik JK. 2018. Ultimate limit state analysis and design of plated structures, 2nd Edition. Chichester, UK: John Wiley & Sons.

Paik JK. 2019. Advanced structural safety studies: with extreme conditions and accidents. Singapore: Springer.

Paik JK, Kim BJ, Park DK, Jang BS. 2011. On quasi-static crushing of thin-walled steel structures in cold temperature: experimental and numerical studies. International Journal of Impact Engineering, 38: 13-28.

Paik JK, Lee DH, Noh SH, Park DK, Ringsberg JW. 2020a. Full-scale collapse testing of a steel stiffened plate structure under cyclic compressive loading. Structures, https://doi.org/10.1016/j.istruc.2020.05.026.

Paik JK, Lee DH, Noh SH, Park DK, Ringsberg JW. 2020b. Full-scale collapse testing of a steel stiffened plate structure under axial compressive loads triggered by brittle fracture at cryogenic condition. Ships and Offshore Structures, https://doi.org/10.1080/17445302.2020.1787930.

Paik JK, Ryu MG, He K, Lee DH, Lee SY, Park DK, Thomas G. 2020c. Full-scale fire testing to collapse of steel stiffened plate structures under lateral patch loading (part 1) – without passive fire protection. Ships and Offshore Structures, https://doi.org/10.1080/17445302.2020.1764705.

Paik JK, Ryu MG, He K, Lee DH, Lee SY, Park DK. 2020d. Thomas G. Full-scale fire testing to collapse of steel stiffened plate structures under lateral patch loading (part 2) – with passive fire protection. Ships and Offshore Structures, http://doi.org/10.1080/17445302.2020.1764706.

Perez-Martin MJ, Holmen JK, Thomesen S, Hopperstad OS, Børvik T. 2019. Dynamic behaviour of a high-strength structural steel at low temperatures. Journal of Dynamic Behavior of Materials. 5: 241-250.

Tanguy B, Besson J, Piques R, Pineau A. 2005a. Ductile to brittle transition of an A508 steel characterized by Charpy impact test: Part I: experimental results. Engineering Fracture Mechanics. 72(1): 49-72.

Tanguy B, Besson J, Piques R, Pineau A. 2005b. Ductile to brittle transition of an A508 steel characterized by Charpy impact test: Part II: modeling of the Charpy transition curve. Engineering Fracture Mechanics. 72(3): 413-434.

Tong L, Niu L, Jing S, Ai L, Zhao, XL. 2018. Low temperature impact toughness of high strength structural steel. Thin-Walled Structures. 132: 410-420.

Yi MS, Lee DH, Lee HH, Paik JK. 2020a. Direct measurements and numerical predictions of welding-induced initial deformations in a full-scale steel stiffened plate structure. Thin-Walled Structures, https://doi.org/10.1016/j.tws.2020.106786.

Yi MS, Noh SH, Lee DH, Seo DH, Paik JK. 2020b. Direct measurements and numerical predictions and simple formula estimations of welding-induced biaxial residual stresses in a full-scale steel stiffened plate structure. Structures, https://doi.org/10.1016/j.istruc.2020.05.030.

Appendix. The test data of the axial compressive load versus axial shortening relation for the tested structure at -80℃.

Load-shortening relation		Stress-strain relation	
Axial compressive load (ton)	Axial shortening (mm)	Stress (MPa)	Strain
0.0000	0.0000	0.0000	0.00000
337.0000	4.5287	79.4704	0.00049
357.4113	4.8390	84.2838	0.00052
378.1256	5.1223	89.1686	0.00056
399.8655	5.4018	94.2952	0.00059
420.4501	5.7010	99.1494	0.00062
441.2043	6.0029	104.0436	0.00065
462.6921	6.2845	109.1108	0.00068
484.2156	6.5727	114.1864	0.00071
506.2856	6.8638	119.3909	0.00074
527.5916	7.1734	124.4152	0.00078
550.2111	7.4323	129.7493	0.00081
571.7793	7.7377	134.8355	0.00084
593.6704	8.0246	139.9978	0.00087
616.0724	8.3067	145.2805	0.00090

637.0315	8.6176	150.2231	0.00093
658.7594	8.9083	155.3469	0.00097
680.7333	9.1776	160.5287	0.00100
702.3568	9.4837	165.6279	0.00103
724.0155	9.7632	170.7354	0.00106
745.0113	10.0704	175.6866	0.00109
767.3142	10.3321	180.9460	0.00112
786.9772	10.6746	185.5828	0.00116
808.8005	10.9291	190.7292	0.00119
828.0775	11.2374	195.2750	0.00122
847.2830	11.5366	199.8040	0.00125
865.6432	11.8523	204.1337	0.00129
883.8128	12.0243	208.4183	0.00130
900.7496	12.3136	212.4123	0.00134
920.4703	12.5379	217.0628	0.00136
935.8377	12.7010	220.6867	0.00138
951.3296	12.9374	224.3400	0.00140
966.6373	13.1308	227.9498	0.00142
981.0017	13.3945	231.3372	0.00145
996.2369	13.6335	234.9299	0.00148
1009.9298	13.8557	238.1589	0.00150
1023.5432	14.1016	241.3692	0.00153
1038.0205	14.3149	244.7832	0.00155
1049.5421	14.6030	247.5002	0.00158
1064.2361	14.7600	250.9653	0.00160
1075.0552	15.0170	253.5166	0.00163
1085.9127	15.2525	256.0770	0.00165
1097.9214	15.4518	258.9089	0.00168
1107.3508	15.6689	261.1325	0.00170
1116.6511	15.8905	263.3257	0.00172
1125.7436	16.1085	265.4698	0.00175
1133.7357	16.3033	267.3545	0.00177
1142.9726	16.4587	269.5327	0.00179
1148.4281	16.7256	270.8192	0.00181
1155.8494	16.8892	272.5693	0.00183
1161.3517	17.0785	273.8668	0.00185
1165.9145	17.2556	274.9428	0.00187
1170.6657	17.4153	276.0632	0.00189
1173.4248	18.0511	276.7139	0.00196
1175.2476	18.2825	277.1437	0.00198
1176.5763	18.4596	277.4571	0.00200
1175.1916	18.6540	277.1305	0.00202
1172.3484	18.8765	276.4600	0.00205

1168.9381	19.1061	275.6558	0.00207
1161.5038	19.3431	273.9027	0.00210
1152.9924	19.5507	271.8956	0.00212
1142.5898	19.8038	269.4425	0.00215
1131.3326	20.0043	266.7878	0.00217
1118.9945	20.2218	263.8783	0.00219
1106.7473	20.4620	260.9902	0.00222
1095.9047	20.6935	258.4333	0.00224
1085.0895	21.1005	255.8829	0.00229
1073.8284	21.6033	253.2273	0.00234
1062.2055	21.9738	250.4864	0.00238
1052.9957	22.2890	248.3146	0.00242
1042.7951	22.5519	245.9091	0.00245
1032.9951	22.8982	243.5981	0.00248
1023.0173	23.1407	241.2452	0.00251
1014.4105	23.3934	239.2155	0.00254
1005.1542	23.6467	237.0328	0.00256
997.6546	23.8152	235.2642	0.00258
989.6032	23.9442	233.3656	0.00260
982.1285	24.5277	231.6029	0.00266
973.3526	24.7959	229.5334	0.00269
964.5549	24.9934	227.4587	0.00271